Ph.D. Dissertation

Search for Supersymmetry in the VBF 0-Lepton Channel at the CMS Experiment and Deep Learning-Based Particle Identification in the Calorimeter

by

YunJae Lee

Department of Physics

The Graduate School of the University of Seoul

August 2025

Search for Supersymmetry in the VBF 0-Lepton Channel at the CMS Experiment and Deep Learning-Based Particle Identification in the Calorimeter

by

YunJae Lee

A Ph.D. Dissertation submitted to the Department of Physics at the Graduate School of the University of Seoul in partial fulfillment of the requirements for the degree of Doctor of Philosophy

June 2025

Approved by

Jason Sanghun Lee

Advisor

This certifies that the Ph.D. Dissertation

of YunJae Lee is approved.

Thesis Committee Chair: Inkyu Park

Thesis Committee Member: Dongsu Bak

Thesis Committee Member: Jason Sanghun Lee

Thesis Committee Member: Hyunsoo Kim

Thesis Committee Member: Junghwan Goh

The Graduate School of the University of Seoul

June 2025

Abstract

Search for Supersymmetry in the VBF 0-Lepton Channel at the CMS Experiment and Deep Learning-Based Particle Identification in the Calorimeter

Supersymmetry (SUSY) is a compelling extension of the Standard Model of particle physics, postulating a symmetry between fermions and bosons to address key issues such as the hierarchy problem and to provide dark matter candidates. A search for SUSY in the vector boson fusion (VBF) 0-lepton channel using data from the Compact Muon Solenoid (CMS) experiment is presented. The VBF topology, characterized by two forward jets with large rapidity separation and minimal central hadronic activity, offers a distinctive environment to probe SUSY scenarios while suppressing Standard Model backgrounds. The analysis targets events with no isolated leptons and significant missing transverse energy, consistent with the production of very soft lepton below measurement threshold and neutral SUSY particles escaping detection. A combination of data-driven techniques and Monte Carlo simulations is employed to estimate key backgrounds, including W/Z+jets and quantum chromodynamics (QCD) multijet processes. The results are interpreted with constraints on superpartner masses and production cross sections of SUSY models.

Deep learning techniques utilizing multivariate features in deep neural networks have been developed for applications in particle physics. In large-scale experiments, handling particle physics data is becoming increasingly complex, and conventional methods are reaching their performance limits while inefficiently utilizing computing resources. The dual-readout calorimeter, with its innate ability to distinguish between electromagnetic and hadronic shower components, presents an opportunity to apply advanced computational methods. To achieve better particle identification and extend the potential of deep learning-based models, a point cloud-based deep learning model is studied that processes three-dimensional shower shapes to identify particles with improved accuracy. In addition to precise energy measurements and timing reconstruction from the two channels, simulation results demonstrate the model's capability in predicting incident energy, direction, and particle types across different conditions. This highlights its potential to enhance calorimetric measurements in future high-energy physics experiments.

Keyword: SUSY, Vector boson fusion, CMS, Dual-readout calorimeter, Particle identification, Deep learning

Ph.D. Dissertation

Search for Supersymmetry in the VBF 0-Lepton Channel at the CMS Experiment and Deep Learning-Based Particle Identification in the Calorimeter

by

YunJae Lee

Department of Physics

The Graduate School of the University of Seoul

August 2025

Contents

List of Figures

List of Tables

Part I

SUSY search in VBF 0-lepton channel at CMS experiment

1. Introduction

The Standard Model of particle physics has been remarkably successful in describing fundamental particles and their interactions. It has withstood decades of experimental verification, including precise tests at the Large Hadron Collider (LHC). However, the Standard Model has well-known shortcomings. It does not account for the nature of dark matter, nor does it provide a natural explanation for the hierarchy problem—the puzzling stability of the Higgs boson mass against large quantum corrections.

The hierarchy problem arises from the quadratic sensitivity of the Higgs boson mass to high-energy scales. In the Standard Model, quantum corrections due to loop diagrams involve contributions from particles up to the Planck scale ($\sim 10^{19}$ GeV), leading to a natural expectation that the Higgs mass should also lie near this scale. However, the observed Higgs mass is only about 125 GeV. Preserving this light mass requires an unnatural fine-tuning of parameters, suggesting that the Standard Model is not complete.

Another major gap in the Standard Model is its inability to explain dark matter, whose presence is inferred from astronomical and cosmological observations. The Standard Model lacks a viable candidate for this form of matter, which must be electrically neutral, massive, and interact only weakly with normal matter.

Supersymmetry (SUSY) is a well-motivated theoretical framework that addresses both of these issues. It introduces a symmetry between fermions and bosons: for every Standard Model particle, there exists a superpartner differing by half a unit of spin. These new particles include squarks (superpartners of quarks), sleptons (superpartners of leptons), gauginos (partners of gauge bosons), and higgsinos (partners of Higgs bosons).

A key benefit of supersymmetry is that contributions from superpartners cancel the divergent quantum corrections to the Higgs mass from their Standard Model counterparts. This stabilizes the Higgs mass at the electroweak scale without requiring fine-tuning. Furthermore, in models where a discrete symmetry called R-parity is conserved, the lightest supersymmetric particle (LSP) is stable. If the LSP is neutral and weakly interacting, as is often the case, it becomes a compelling dark matter candidate.

Probing for supersymmetric particles requires extremely high energies, which makes the LHC an essential tool. The Compact Muon Solenoid (CMS) experiment, one of the general-purpose detectors at the LHC, plays a central role in these searches. While many supersymmetric models with large mass splittings have already been ruled out, more challenging scenarios remain—particularly those with compressed mass spectra, where decay products are soft and thus harder to detect.

In compressed spectra, the small mass differences between particles lead to final states with low-momentum objects, often below detector thresholds. Such scenarios are well-motivated in natural SUSY models, especially those where the LSP is Higgsino-like. These configurations also produce an appropriate relic dark matter density through co-annihilation processes.

To enhance sensitivity to compressed SUSY spectra, this thesis focuses on the Vector Boson Fusion (VBF) topology. VBF processes involve the emission of two vector bosons (W or Z) from incoming quarks, which subsequently fuse to produce a heavy particle. These events are characterized by two forward jets with large rapidity separation and low hadronic activity in the central region. This clean event topology helps suppress Quantum Chromodynamics (QCD) backgrounds, which typically feature more central activity.

Compressed SUSY decays can produce leptons that are too soft to be detected. Therefore, the 0-lepton channel—events with no reconstructed electrons or muons—is particularly effective in this search. In the absence of leptons, backgrounds from processes such as W+jets and top quark pair production are significantly reduced. Events in this channel often exhibit large missing transverse energy, due to the LSP escaping undetected, making it a powerful signature for SUSY.

The goal of this thesis is to search for supersymmetric particles in the VBF topology using the 0-lepton channel at CMS. The analysis is particularly sensitive to compressed electroweakino spectra, which remain largely unexplored by previous searches and offer a compelling target for new physics.

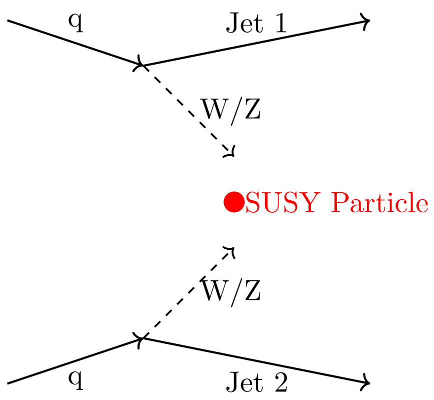

Figure 1.1: Schematic representation of a SUSY particle produced via the Vector Boson Fusion (VBF) process.

2. Theoretical Background

2.1 Standard Model

The Standard Model [2] is a comprehensive theory describing fundamental particles of matter and the interactions between them. It categorizes particles into two families: quarks and leptons. Quarks come in six types (up, down, charm, strange, top, bottom) and combine to form protons and neutrons. Leptons include the electron, muon, tau, and their associated neutrinos.

Interactions among these particles are mediated by gauge bosons. Photons mediate the electromagnetic force, W and Z bosons mediate the weak force, and gluons mediate the strong force. Additionally, the Higgs boson is responsible for giving mass to particles through the Higgs mechanism, a process associated with electroweak symmetry breaking.

Gauge invariance is a fundamental principle of the Standard Model, requiring that the laws of physics remain unchanged under local transformations of certain fields. This principle gives rise to the gauge bosons and dictates the structure of particle interactions. Electroweak symmetry breaking refers to the phenomenon where the unified electroweak force separates into distinct electromagnetic and weak forces, mediated by the Higgs field acquiring a nonzero vacuum expectation value.

Quantum corrections refer to the modifications in the values of particle properties, such as masses and couplings, arising from the effects of virtual particles fluctuating in and out of existence according to the rules of quantum mechanics. These corrections can be large for the observed Higgs boson mass, leading to the hierarchy problem.

The Planck scale, around 10^{19} GeV, represents the energy scale where gravitational forces become as strong as other fundamental forces, and quantum effects of gravity cannot be neglected. In the Standard Model without new physics, the Higgs boson mass would naturally be driven towards this very high energy scale, requiring severe fine-tuning to remain at the measured value of about 125 GeV.

Furthermore, cosmological observations necessitate the existence of dark matter, a form of matter that does not interact strongly with normal matter and remains unexplained within the Standard Model. Additionally, the observed baryon asymmetry (imbalance between matter and antimatter) and the non-zero neutrino masses suggest new physics beyond the Standard Model.

Finally, gauge coupling constants, which describe the strengths of fundamental forces, do not unify at a high energy within the Standard Model, suggesting the need for an extended framework.

Gauge couplings quantify the strength of each fundamental interaction. In the Standard Model, the coupling constants of the electromagnetic, weak, and strong forces evolve differently as energy increases. Although they become closer at higher energies, they do not meet exactly at a single point. This lack of unification suggests that the Standard Model might only be an effective low-energy theory and that new physics, such as supersymmetry, could unify the forces at a grand unified scale.

2.2 Supersymmetry

2.2.1 Concept and Hierarchy Problem

Supersymmetry (SUSY) is a theoretical framework that extends the Standard Model by proposing a symmetry between fermions (particles with half-integer spin, such as electrons and quarks) and bosons (particles with integer spin, like photons and gluons). Each particle from the Standard Model is paired with a superpartner that differs in spin by half-integer values: fermions have scalar superpartners (selectrons, squarks), and gauge bosons have fermionic superpartners (photinos, gluinos). SUSY effectively addresses the hierarchy problem by having bosonic and fermionic quantum corrections naturally cancel each other out, significantly stabilizing the Higgs boson mass.

SUSY addresses several critical theoretical challenges. First, it provides a natural solution to the hierarchy problem by stabilizing the Higgs boson mass against large quantum corrections. Second, SUSY promotes gauge coupling unification. When supersymmetric particles are included in the evolution of gauge couplings with energy, the couplings converge much more precisely at a high energy scale.

Furthermore, SUSY offers a compelling dark matter candidate. The lightest supersymmetric particle (LSP), stabilized by R-parity conservation, is typically neutral and weakly interacting, making it an excellent candidate for cold dark matter observed in the universe.

Experimental searches for SUSY proceed along several lines. Direct searches at high-energy colliders like the Large Hadron Collider (LHC) seek to produce supersymmetric particles and identify their decay patterns, often involving missing transverse energy ($E_{\mathrm{T}}^{\mathrm{miss}}$) signatures. Indirect searches involve precision measurements of Standard Model processes where SUSY effects could cause small deviations. Additionally, astrophysical observations and underground experiments attempt to detect dark matter particles through their rare interactions with ordinary matter, potentially revealing evidence for the LSP predicted by SUSY.

2.2.2 The Minimal Supersymmetric Standard Model

The Minimal Supersymmetric Standard Model (MSSM) [3] represents the simplest and most practical SUSY extension of the Standard Model. It includes superpartners for every Standard Model particle and introduces two distinct Higgs fields (H_u for up-type fermions and H_d for down-type fermions). These additional Higgs fields help achieve anomaly cancellation and enable electroweak symmetry breaking, producing five observable Higgs bosons. To remain consistent with current experimental observations, MSSM includes "soft" SUSY-breaking terms, ensuring the superpartners' masses exceed current detection thresholds while preserving the attractive theoretical solutions offered by SUSY.

2.2.3 R-Parity and the Lightest Supersymmetric Particle

Many SUSY models incorporate a quantum number called R-parity (R_P), defined as $R_P = (-1)^{3(B-L)+2s}$, with baryon number (B), lepton number (L), and spin (s). Standard Model particles have $R_P = +1$, while their superpartners have $R_P = -1$. R-parity conservation implies that superpartners must be produced in pairs and ensures the stability of the LSP. Typically, the LSP is electrically neutral and weakly interacting, making it undetectable directly and resulting in a significant missing transverse energy ($E_{\mathrm{T}}^{\mathrm{miss}}$) signal in detectors. Due to its stable and elusive nature, the LSP is a natural candidate for dark matter, aligning SUSY predictions with cosmological data.

2.2.4 SUSY-Breaking and Compressed Spectra

Since our universe consists of non-SUSY particle, exact SUSY symmetry is experimentally excluded, so mechanisms that softly break SUSY must be introduced. Common SUSY-breaking mechanisms include gravity-mediated, gauge-mediated, and anomaly-mediated SUSY breaking. Gravity-mediated SUSY breaking involves gravitational interactions at high energies, gauge-mediated breaking uses gauge interactions at intermediate energies, and anomaly-mediated breaking relies on quantum corrections related to anomalies. These mechanisms increase the mass of the superpartners, placing them beyond direct experimental reach.

Particularly challenging are "compressed spectra" scenarios, where mass differences between superpartners are minimal (on the order of tens of GeV or less). Such compressed scenarios lead to decay products with very low momentum, evading traditional detection techniques based on high-energy leptons or jets. These scenarios instead rely on global event characteristics such as significant missing transverse energy, necessitating tailored detection strategies.

2.3 Vector–Boson Fusion Production

Vector-boson fusion (VBF) is a particularly advantageous production channel for supersymmetry (SUSY) searches, especially in scenarios where the superpartner mass spectrum is compressed. In such cases, the decay products of SUSY particles often have low momentum and may not pass conventional trigger thresholds that rely on energetic leptons or jets.

VBF events are characterized by two incoming quarks that each radiate an electroweak gauge boson. These bosons fuse into a heavy neutral state, while the scattered quarks appear as two energetic jets in the forward regions of the detector. The resulting topology features: - Two high-p_T forward jets with a large pseudorapidity separation, - Suppressed hadronic activity in the central region, - And moderate missing transverse energy ($E_{\mathrm{T}}^{\mathrm{miss}}$) from invisible particles such as the LSP.

This VBF topology benefits SUSY searches in multiple ways. First, the forward jets help the events pass both hardware and software triggers, even when the SUSY system itself produces soft decay products. Second, the absence of color exchange between the two quark lines leads to minimal hadronic activity in the central region—an effect known as color coherence. This suppression of central jets distinguishes VBF events from background processes like QCD multijet production or top-quark decays, which typically produce more central jets.

In compressed-spectrum SUSY models, the LSP carries away energy invisibly, producing a modest but nonzero $E_{\mathrm{T}}^{\mathrm{miss}}$ signature. When this missing energy is combined with the forward-jet configuration and central jet veto, VBF becomes a powerful and clean channel for isolating electroweak SUSY production from Standard Model backgrounds.

2.4 Expected Signatures and Backgrounds

In a SUSY search using the VBF channel with no detected leptons (0-lepton channel), key experimental signatures include two widely separated forward jets, substantial missing transverse energy, reduced central activity and absence of isolated leptons. The main backgrounds in these analyses come from Standard Model processes like $Z(\nu\bar{\nu})$ events with jets, $W(\ell\nu)$ events with undetected leptons, and QCD multijet events involving mismeasured jet energies. Effective control and precise estimation of these backgrounds rely on carefully designed control regions—specific detector regions dominated by known processes—and data-driven methods, using actual collision data to accurately predict background contributions in the signal region. Detailed methods and results from these approaches are further explored in Chapter 4.

3. Experimental Setup

High-energy physics relies on powerful particle accelerators and highly sophisticated detectors to explore the fundamental structure of matter. This chapter provides an overview of the Large Hadron Collider (LHC), where high-energy collisions are produced, and the Compact Muon Solenoid (CMS), one of its flagship detectors. Understanding the experimental setup is essential for interpreting the collision data and identifying new phenomena.

3.1 Large Hadron Collider (LHC)

The Large Hadron Collider (LHC) [4] is the world's most powerful particle accelerator at CERN (the European Organization for Nuclear Research), designed for exploring fundamental questions in particle physics. The LHC accelerates two proton beams in opposite directions around a 27-kilometer ring using a series of superconducting magnets and radio frequency cavities. Protons are particularly suitable for acceleration due to their electric charge, allowing them to be guided effectively by magnetic fields.

Each proton beam is accelerated to an energy of 6.5 TeV, resulting in a center-of-mass energy of 13 TeV when the beams collide. During these collisions, the constituent particles of the proton—quarks and gluons—interact at very short distances and high energies, producing a wide variety of final-state particles. These collisions simulate conditions that existed moments after the Big Bang.

The LHC achieves high collision rates through its remarkable instantaneous luminosity, which quantifies the number of collisions per unit area per second. This is essential for accumulating enough data to observe rare processes like SUSY particle production. Precision alignment, sophisticated beam monitoring systems, and cryogenic infrastructure allow the LHC to maintain stable high-energy collisions over extended periods, enabling large-scale data collection for CMS and other experiments.

3.2 Compact Muon Solenoid (CMS)

The Compact Muon Solenoid (CMS) [5] is one of the two large general-purpose particle detectors at the LHC. Designed to investigate a wide range of physics phenomena—including the search for the Higgs boson, supersymmetry (SUSY), and extra dimensions—CMS plays a crucial role in advancing our understanding of fundamental particles and forces.

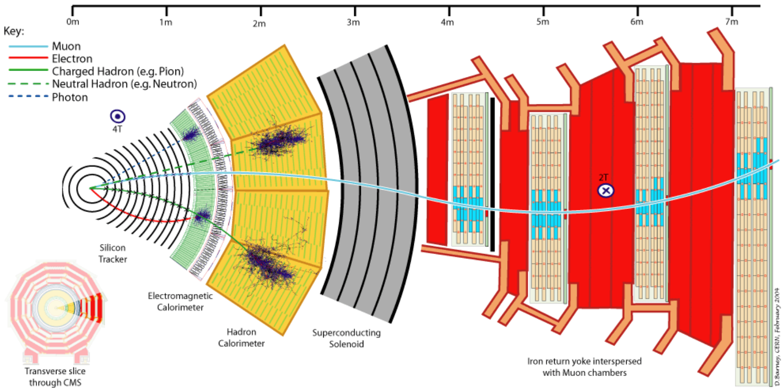

Figure 3.1: Slice of the CMS detector.[1]

As illustrated in Figure 3.1, the detector consists of several layers of subdetectors arranged concentrically around the beam axis, each specialized for detecting different types of particles produced in proton-proton collisions. This design allows for comprehensive measurement and identification of particles over a wide range of energies and directions.

CMS is designed to provide high-resolution measurements of particle trajectories, energies, and identities. Its hermetic coverage ensures that nearly all particles produced in collisions are detected or accounted for, allowing for accurate measurements of missing transverse energy—a key signature in searches for particles that escape detection, such as the lightest supersymmetric particle. The synergy between the detector's subsystems enables CMS to reconstruct complex final states with high efficiency and precision.

Tracker

The tracker is the innermost subdetector of CMS and is critical for reconstructing the trajectories of charged particles emerging from the collision point. It consists of a central pixel detector surrounded by multiple layers of silicon strip detectors, covering a pseudorapidity range of $|\eta| < 2.5$. The high spatial resolution of the silicon sensors allows for precise measurements of particle trajectories.

By measuring the curvature of charged particle tracks in the magnetic field, the tracker determines their momenta with high precision. It also plays a vital role in identifying the primary interaction vertex and detecting secondary vertices from the decays of short-lived particles, such as B mesons. This capability is essential for flavor physics studies and searches for heavy particles.

Calorimeters

The CMS calorimetry system is designed to measure the energies of electrons, photons, and hadrons. It consists of two main components:

Electromagnetic Calorimeter (ECAL)

The ECAL is a calorimeter made of lead tungstate ($PbWO_4$) crystals, which scintillate when traversed by high-energy electrons or photons. It covers a pseudorapidity range of $|\eta| < 3.0$ and provides excellent energy resolution due to the high density, short radiation length, and fast scintillation response of the crystals.

The ECAL is segmented into a barrel region covering $|\eta| < 1.48$ and two endcap regions covering $1.48 < |\eta| < 3.0$. Precision energy measurements from the ECAL are crucial for identifying electrons and photons and for reconstructing their energies in physics analyses. The ECAL achieves an energy resolution better than 1% for high-energy electrons and photons, making it essential for precision measurements in Higgs and SUSY studies.

Hadronic Calorimeter (HCAL)

Surrounding the ECAL, the HCAL is designed to measure the energies of hadrons, such as pions, kaons, and protons. It is a sampling calorimeter composed of layers of brass absorber interleaved with plastic scintillator tiles. The HCAL covers a pseudorapidity range of $|\eta| < 3.0$, with additional forward calorimeters extending the coverage to $|\eta| < 5.2$.

The HCAL measures the energy deposited by hadronic showers, providing essential information for the reconstruction of jets and missing transverse energy (MET), which are key signatures in many physics analyses, including searches for SUSY.

3.2.1 Superconducting Solenoid Magnet

The superconducting solenoid magnet is a central feature of CMS, measuring 13 m in length and 6 m in diameter. It generates a magnetic field of 3.8 T, which is contained within the magnet yoke to minimize stray fields. The magnet is located between the calorimeters and the muon system. The strong magnetic field is essential for bending the paths of charged particles, enabling precise momentum measurements by the inner tracker and the muon system.

3.2.2 Muon System

The muon system is the outermost sub-detector of CMS and is dedicated to detecting muons—minimally ionizing, highly penetrating particles capable of traversing significant amounts of material with minimal energy loss. It consists of several types of gaseous detectors: GEM, RPCs, CSC. These detectors provide precise position and timing measurements for muon tracks. Combined with the momentum measurements from the inner tracker and the magnetic field, the muon system allows for accurate reconstruction of muon trajectories and momenta. Muons are important probes in many physics analyses due to their clean signatures and relatively low backgrounds.

3.2.3 Trigger and Data Acquisition System

The CMS trigger and data acquisition system is designed to efficiently select interesting events from the vast number of proton-proton collisions occurring at the LHC, which can reach rates of up to 40 MHz. The trigger system operates in two stages:

Level-1 Trigger (L1): A hardware-based system using custom electronics to make fast decisions (within about 4 μs) based on coarse information from the calorimeters and muon detectors. It reduces the event rate to about 100 kHz.

High-Level Trigger (HLT): A software-based system running on a computing farm that performs more detailed event reconstruction and selection, reducing the event rate further to about 1 kHz for storage and offline analysis.

Without an efficient trigger system, the vast majority of data from proton-proton collisions would be lost due to limitations in storage and processing. SUSY events are rare and often look similar to Standard Model backgrounds, so the trigger system is carefully optimized to retain events with features such as large missing energy, high-p_T jets, or isolated leptons, which may indicate the presence of new physics.

4. Analysis

4.1 Analysis Dataset

This analysis utilizes proton-proton collision data collected with the CMS detector at the Large Hadron Collider (LHC) during Run 2 (2016–2018), corresponding to an integrated luminosity of approximately 137 fb^{-1}. Events are selected using MET-based triggers, with year-specific thresholds optimized to maintain high efficiency for events exhibiting significant missing transverse energy ($E_{\mathrm{T}}^{\mathrm{miss}}$). These triggers are particularly effective for SUSY searches in the 0-lepton channel, where the signature of new physics is large $E_{\mathrm{T}}^{\mathrm{miss}}$ due to undetected neutral particles.

The analysis targets final states with large $E_{\mathrm{T}}^{\mathrm{miss}}$ and no isolated leptons, consistent with supersymmetric (SUSY) models in which the Lightest Supersymmetric Particle (LSP) escapes detection. These scenarios include compressed spectra and decay chains initiated through vector boson fusion (VBF). Both real data and Monte Carlo (MC) simulations are used for signal and background estimation.

4.1.1 Signal Monte Carlo Samples

Signal events are generated using simplified SUSY models designed to represent key production and decay topologies relevant to the VBF 0-lepton channel. Event generation is performed with MadGraph for matrix-element calculations and Pythia for parton showering and hadronization. Detector simulation is based on the GEANT4-based CMS software framework.

The scenarios of interest include:

- **Wino-Bino Model:** Chargino-neutralino production ($\tilde{\chi}_1^{\pm}\tilde{\chi}_2^0$) followed by decays through off-shell W and Z bosons. The neutralino LSP is stable and escapes detection, resulting in final states with large $E_{\mathrm{T}}^{\mathrm{miss}}$. Leptonic decays of the W/Z are often undetectable due to compression in mass spectrum.

- **Higgsino Model:** Nearly mass-degenerate $\tilde{\chi}_1^{\pm}$, $\tilde{\chi}_2^0$, and $\tilde{\chi}_1^0$ states. Decays produce very soft visible particles, typically below reconstruction thresholds, leading to pure $E_{\mathrm{T}}^{\mathrm{miss}}$ signatures. This topology is enhanced in the VBF production mode.

- **Stau Coannihilation Model:** In some scenarios, the $\tilde{\tau}_1$ is nearly degenerate with the $\tilde{\chi}_1^0$, and decays result in low-energy tau leptons. Although visible taus are vetoed in this analysis, the model is still relevant if taus are not reconstructed or are below detection thresholds.

All SUSY signal samples are generated with an explicit requirement of two forward jets at the generator level to model the VBF topology. Mass points are chosen to scan the SUSY parameter space, with emphasis on configurations leading to large $E_{\mathrm{T}}^{\mathrm{miss}}$ and forward jet characteristics. The samples are normalized using next-to-leading-order (NLO) or next-to-next-to-leading-order (NNLO) theoretical cross-sections.

4.1.2 Background Monte Carlo Samples

Standard Model (SM) background processes that can mimic the SUSY signal are modeled using MC simulations and include:

- $Z(\nu\bar{\nu})$ + jets: Irreducible background with genuine $E_{\mathrm{T}}^{\mathrm{miss}}$ from neutrinos.
- $W(\ell\nu)$ + jets: Mimics signal when leptons are undetected.
- QCD multijet: Can fake $E_{\mathrm{T}}^{\mathrm{miss}}$ due to jet mismeasurements.
- Top quark production ($t\bar{t}$ and single top): Backgrounds from events with neutrinos and b-jets.
- Diboson production (WW, WZ, ZZ): Contains $E_{\mathrm{T}}^{\mathrm{miss}}$ and jets.

- Rare processes: Includes triboson and $t\bar{t}+V$ production.

All samples undergo full CMS detector simulation and are reconstructed using the same software as real data. Background modeling is validated using control regions and corrected using data-to-MC scale factors.

4.1.3 Observables

To distinguish SUSY signals from Standard Model backgrounds, a set of carefully chosen observables are employed. These observables reflect the underlying event topology and kinematics associated with VBF production and invisible particles:

- **Jet Transverse Momentum (p_T)**: Measures the transverse energy of each reconstructed jet. High p_T jets are indicative of energetic parton interactions. In VBF events, the leading and subleading jets are expected to have significant p_T, and a threshold (typically >30–50 GeV) is applied.

- **Pseudorapidity (η)** and **Azimuthal Angle (ϕ)**: η measures the angle of a jet with respect to the beam axis, while ϕ measures the angle in the transverse plane. These quantities help to define the jet direction and allow calculation of the $\Delta\eta$ separation and angular correlations in the event.

- **Dijet Invariant Mass (m_{jj})**: Constructed from the two highest-p_T jets, this variable captures the mass of the system formed by the forward jets. A large m_{jj} (typically >500 GeV) is a hallmark of VBF events due to the large momentum transfer from the initial quarks.

- **Pseudorapidity Gap ($\Delta\eta$)**: The absolute difference in pseudorapidity between the two leading jets, $\Delta\eta = |\eta_1 - \eta_2|$. A large $\Delta\eta$ (>3.8–4.0) ensures selection of events with widely separated jets, consistent with t-channel VBF topology.

- **Central Jet Multiplicity**: Counts additional jets between the two VBF-tagging jets in η. Events with central jets are vetoed to reduce backgrounds from QCD and top quark processes, where radiation or decay products often populate the central region.

- **Missing Transverse Energy ($E_{\mathrm{T}}^{\mathrm{miss}}$)**: Represents the imbalance in total transverse momentum and is a key signature of undetected particles, such as neutrinos or the LSP. A high $E_{\mathrm{T}}^{\mathrm{miss}}$ threshold (e.g., >250 GeV) is applied to suppress SM backgrounds and enhance sensitivity to SUSY.

- **Angular Variables ($|\Delta\phi(E_{\mathrm{T}}^{\mathrm{miss}}, j)|$)**: The azimuthal angle between the $E_{\mathrm{T}}^{\mathrm{miss}}$ vector and the jets is used to suppress QCD multijet events. In genuine $E_{\mathrm{T}}^{\mathrm{miss}}$ events, $E_{\mathrm{T}}^{\mathrm{miss}}$ is not aligned with jets, so requiring

$|\Delta\phi| > 0.5$ removes events where the imbalance arises from jet mismeasurement.

These observables serve as inputs for both traditional cut-based event selection and multivariate analyses (e.g., BDTs or DNNs), maximizing signal-to-background separation.

4.2 Event Selection

To isolate SUSY signal events from SM backgrounds, selection criteria exploit VBF topology and $E_{\mathrm{T}}^{\mathrm{miss}}$ signatures. Events must pass MET triggers and a primary vertex requirement. Core selection elements include:

- **Trigger Selection**: Events are required to pass MET triggers such as `HLT_PFMETNoMu120_PFMHTNoMu120_IDTight`, which are highly efficient for events with genuine missing energy.

- **Primary Vertex Requirement**: A reconstructed primary vertex with good quality is required to ensure events originate from a real collision.

- **Lepton Vetoes**: Events containing isolated electrons, muons, or hadronically decaying taus are rejected to suppress W and Z boson backgrounds. Identification criteria include relative isolation (I_{rel}), pseudorapidity acceptance, and object-specific ID algorithms (e.g., medium cut-based for electrons, DeepTau for taus). tight anti-e/μ discrimination and prongs to satisfying 1 or 3 Hadrons + Strips(HPS).

- ***b*-Jet Veto**: Events containing b-tagged jets are excluded using the medium working point of the DeepCSV algorithm. This reduces background from top quark production.
- **High $E_{\mathrm{T}}^{\mathrm{miss}}$ Cut**: A threshold of $E_{\mathrm{T}}^{\mathrm{miss}} > 250$ GeV is applied to isolate events with significant imbalance in transverse energy.
- **QCD Suppression**: The angular separation $|\Delta\phi(E_{\mathrm{T}}^{\mathrm{miss}}, j)|$ between the $E_{\mathrm{T}}^{\mathrm{miss}}$ and the leading jets must be greater than 0.5, suppressing events where $E_{\mathrm{T}}^{\mathrm{miss}}$ originates from mismeasured jets.
- **Jet Selection**: At least two jets with $p_T > 30$ GeV and $|\eta| < 4.7$ are required. Jet identification quality is enforced using loose or tight working points depending on the data-taking year.
- **VBF Dijet Topology**: The two leading jets must have an invariant mass $m_{jj} > 500$ GeV and be separated by $\Delta\eta > 3.8$, and be in opposite hemispheres ($\eta_1 \cdot \eta_2 < 0$).

These selection criteria are optimized using simulated signal and background samples to maximize signal significance. Control regions are defined by inverting one or more of these selections to validate the modeling of backgrounds in data.

Step	Object	Selection Cuts
Central	Trigger	`HLT_PFMETNoMu120_PFMHTNoMu120_IDTight`
	e veto	$N(e) = 0,\ p_{\mathrm{T}}(e) > 5$ GeV, $\lvert\eta(e)\rvert < 2.1,\ I_{rel} < 0.15$, medium cut-based ID
	μ veto	$N(\mu) = 0,\ p_{\mathrm{T}}(\mu) > 3$ GeV, $\lvert\eta(\mu)\rvert < 2.1,\ I_{rel} < 0.15$, tight particle-flow ID
	τ veto	$N(\tau) = 0,\ p_{\mathrm{T}}(\tau) > 20$ GeV, $\lvert\eta(\tau)\rvert < 2.1$, tight anti-$e/\mu$ discrimination, prong = 1 or 3 (HPS)
	b-jet veto	$N(b) = 0,\ p_{\mathrm{T}}(b) > 30$ GeV, $\lvert\eta(b)\rvert < 2.4$, medium DeepCSV WP
	$E_{\mathrm{T}}^{\mathrm{miss}}$	$E_{\mathrm{T}}^{\mathrm{miss}} > 250$ GeV
	QCD rejection	$\lvert\Delta\phi(E_{\mathrm{T}}^{\mathrm{miss}}, j)\rvert_{\min} > 0.5,\ p_{\mathrm{T}}(j) > 30\ GeV,\ \lvert\eta(j)\rvert < 4.7$, loose ID (2016)/ tight ID (2017–2018)
VBF	Jet selection	$N(j) \geq 2,\ p_{\mathrm{T}}(j) > 30$ GeV, $\lvert\eta(j)\rvert < 4.7$, loose ID (2016) / tight ID (2017–2018)
	Dijet selection	$\Delta\eta(j_1, j_2) > 3.8,\ \eta(j_1) \cdot \eta(j_2) < 0,\ m_{jj} > 500$ GeV

Table 4.1: Summary of signal region selection criteria by object.

4.3 Background Estimation

the dominant backgrounds in the 0-lepton channel arises from the production of a Z boson in association with jets, where the Z decays into neutrinos, resulting in genuine missing transverse momentum ($E_{\mathrm{T}}^{\mathrm{miss}}$). Since neutrinos are not directly detectable, these events are irreducible and closely mimic the SUSY signal signature. To estimate this background in a data-driven way, events in which the Z boson decays into a pair of muons are used as a proxy.

In the selected $Z(\mu^+\mu^-)$ control region, the two muons are treated as invisible by adding their transverse momenta to the original missing transverse momentum of the event. This yields a recalculated quantity:

$$\vec{p}_T^{\text{miss, recalculated}} = \vec{p}_T^{\text{miss}} + \vec{p}_T^{\mu^+} + \vec{p}_T^{\mu^-}, \tag{4.1}$$

which emulates the $E_{\mathrm{T}}^{\mathrm{miss}}$ distribution expected from $Z(\nu\bar{\nu})$ events. This method allows for the prediction of the kinematic distributions in the signal region using data alone, without relying on $Z(\nu\bar{\nu})$ Monte Carlo samples. The control region selection is otherwise identical to the signal region, except for the requirement of two well-identified muons within the Z mass window. Systematic uncertainties associated with acceptance, reconstruction efficiency, and residual differences between the two decay channels are considered in the final estimate.

4.3.1 $Z(\nu\bar{\nu})$ + Jets

$SF_{BG}^{Cut} = \frac{N_{Data}^{Cut} - \Sigma N_{MC\ \ non-BG}^{Cut}}{N_{MC\ \ BG}^{Cut}}$ $SF_{BG}^{Central\,\&\,VBF} = SF_{BG}^{Central} \cdot SF_{BG}^{VBF}$ $N_{BG}^{Central\,\&\,VBF} = N_{MC\ \ BG}^{Central\,\&\,VBF} \cdot SF_{BG}^{Central} \cdot SF_{BG}^{VBF}$

In this region, mismodeling effects related to jet energy response and jet multiplicity can affect the extrapolation. A correction is applied to account for differences in the Z boson p_T spectrum between data and simulation. Figure **??** shows the data-to-MC ratio before and after applying the Z boson

p_T reweighting. The discrepancy is more pronounced at high p_T, and the reweighting improves agreement across the spectrum.

Step	**Object**	**Selection Cuts**
Central	Trigger	`HLT_IsoMu24 (2016, 2018)`, `HLT_IsoMu27 (2017)`
	μ selection	$N(\mu) \geq 2$, $p_{\mathrm{T}}(\mu) > 30$ GeV, $\lvert\eta(\mu)\rvert < 2.1$, $I_{rel} < 0.15$, tight particle-flow ID
	Additional μ veto	$N(\mu) = 0$, 3 GeV $< p_{\mathrm{T}}(\mu) < 30$ GeV, $\lvert\eta(\mu)\rvert < 2.1$, $I_{rel} < 0.15$, tight particle-flow ID
	e veto	$N(e) = 0$, $p_{\mathrm{T}}(e) > 5$ GeV, $\lvert\eta(e)\rvert < 2.1$, medium cut-based ID
	τ veto	$N(\tau) = 0$, $p_{\mathrm{T}}(\tau) > 20$ GeV, $\lvert\eta(\tau)\rvert < 2.1$, tight anti-$e/\mu$ discrimination, prong = 1 or 3 (HPS), $\Delta R(\tau_h, e/\mu) > 0.3$, DeepTau2017v2p1, tight isolation
	b-jet veto	$N(b) = 0$, $p_{\mathrm{T}}(b) > 30$ GeV, $\lvert\eta(b)\rvert < 2.4$, medium DeepCSV working point
	$E_{\mathrm{T}}^{\mathrm{miss}}$	$E_{\mathrm{T}}^{\mathrm{miss}} > 250$ GeV
	QCD rejection	$\lvert\Delta\phi(E_{\mathrm{T}}^{\mathrm{miss}}, j)\rvert_{\mathrm{min}} > 0.5$, $p_{\mathrm{T}}(j) > 30\ GeV$, $\lvert\eta(j)\rvert < 4.7$, loose ID (2016)/ tight ID (2017–2018)
VBF	Jet selection	$N(j) \geq 2$, $p_{\mathrm{T}}(j) > 30$ GeV, $\lvert\eta(j)\rvert < 4.7$, loose ID (2016) / tight ID (2017–2018)
	Dijet selection	$\Delta\eta(j_1, j_2) > 3.8$, $\eta(j_1) \cdot \eta(j_2) < 0$, $m_{jj} > 500$ GeV

Table 4.2: Summary of control region selection criteria for Z+jets background estimation.

4.3.2 $W(\ell\nu)$ + Jets

Backgrounds from W bosons are estimated using a single-lepton control region. The estimation accounts for lepton identification and isolation efficiencies, as well as extrapolation to events where the lepton is not reconstructed or falls outside the detector acceptance. As with the Z+jets background, a boson p_T-based scale factor is applied to correct for mismodeling in the W boson p_T spectrum.

Sample	**2016**	**2017**	**2018**
QCD	0.0 ± 0.0	0.0 ± 0.0	0.0 ± 0.0
W+Jets	0.0 ± 0.0	0.1 ± 0.0	0.0 ± 0.0
Single top	2.8 ± 0.7	1.2 ± 0.5	2.0 ± 0.8
$t\bar{t}$	19.3 ± 1.0	16.5 ± 1.0	27.2 ± 1.5
Rares	30.3 ± 2.5	17.7 ± 0.9	22.5 ± 1.7
Diboson	39.7 ± 1.9	31.9 ± 1.8	52.1 ± 2.5
EWK V	97.2 ± 3.7	80.4 ± 3.9	129.4 ± 6.0
Z+Jets	792.1 ± 11.0	865.8 ± 12.0	1296.4 ± 16.3
Total MC	981.4 ± 12.1	1013.6 ± 12.8	1529.6 ± 17.7
Data	1130	1019	1463
Data / MC	1.151 ± 0.037	1.005 ± 0.034	0.956 ± 0.027
Purity [%]	80.7	85.4	84.8
SF (central+VBF)	1.269 ± 0.050	1.075 ± 0.043	1.061 ± 0.037

Table 4.3: Z+Jet background estimation Event yields and scale factors for the CMS VBF SUSY analysis across 2016–2018.

Although this scale factor is not empirically derived from W boson events, it is borrowed from the Z boson reweighting procedure under the assumption of similar kinematic effects. Figure **??** demonstrates the improvement in the data-to-MC ratio in the W+jets control region after applying the correction.

4.3.3 QCD Multijet Background

Although QCD multijet events generally do not produce genuine $E_{\mathrm{T}}^{\mathrm{miss}}$, fluctuations in jet energy measurements can result in significant fake $E_{\mathrm{T}}^{\mathrm{miss}}$. A data-driven ABCD method is employed to estimate the QCD background. This method defines four regions based on cuts in two variables that are assumed to be approximately uncorrelated in QCD-dominated samples. Under

Step	**Object**	**Selection Cuts**
Central	Trigger	`HLT_IsoMu24 (2016, 2018)`, `HLT_IsoMu27 (2017)`
	μ selection	$N(\mu) = 1$, $p_{\mathrm{T}}(\mu) > 30$ GeV, $\lvert\eta(\mu)\rvert < 2.1$, $I_{rel} < 0.15$, $60\ GeV < m_T(\mu, p_{\mathrm{T}}^{\mathrm{miss}}) < 100\ GeV$, tight particle-flow ID
	Additional μ veto	$N(\mu) = 0$, 3 GeV $< p_{\mathrm{T}}(\mu) < 30$ GeV, $\lvert\eta(\mu)\rvert < 2.1$, $I_{rel} < 0.15$, tight particle-flow ID
	e veto	$N(e) = 0$, $p_{\mathrm{T}}(e) > 5$ GeV, $\lvert\eta(e)\rvert < 2.1$, medium cut-based ID
	τ veto	$N(\tau) = 0$, $p_{\mathrm{T}}(\tau) > 20$ GeV, $\lvert\eta(\tau)\rvert < 2.1$, tight anti-$e/\mu$ discrimination, prong = 1 or 3 (HPS), $\Delta R(\tau_h, e/\mu) > 0.3$, DeepTau2017v2p1, tight isolation
	b-jet veto	$N(b) = 0$, $p_{\mathrm{T}}(b) > 30$ GeV, $\lvert\eta(b)\rvert < 2.4$, medium DeepCSV working point
	$E_{\mathrm{T}}^{\mathrm{miss}}$	$E_{\mathrm{T}}^{\mathrm{miss}} > 250$ GeV
	QCD rejection	$\lvert\Delta\phi(E_{\mathrm{T}}^{\mathrm{miss}}, j)\rvert_{\min} > 0.5$, $p_{\mathrm{T}}(j) > 30\ GeV$, $\lvert\eta(j)\rvert < 4.7$, loose ID (2016)/ tight ID (2017–2018)
VBF	Jet selection	$N(j) \geq 2$, $p_{\mathrm{T}}(j) > 30$ GeV, $\lvert\eta(j)\rvert < 4.7$, loose ID (2016) / tight ID (2017–2018)
	Dijet selection	$\Delta\eta(j_1, j_2) > 3.8$, $\eta(j_1) \cdot \eta(j_2) < 0$, $m_{jj} > 500$ GeV

Table 4.4: Summary of control region selection criteria for W+jets background estimation.

this assumption, the event yields satisfy the relation $N_A : N_B = N_C : N_D$, allowing the prediction of the QCD yield in the signal-like region as $N_A = N_B \cdot \frac{N_C}{N_D}$.

For QCD multijet background estimation, we choose $E_{\mathrm{T}}^{\mathrm{miss}}$ and the minimum azimuthal separation between the leading two jets and $E_{\mathrm{T}}^{\mathrm{miss}}$, $|\Delta\phi(\vec{p}_T^{\mathrm{miss}}, j|_{\min}$, as the two variables. While the magnitude of $E_{\mathrm{T}}^{\mathrm{miss}}$ is influenced by the extent of jet energy mismeasurements, the ϕ direction of $E_{\mathrm{T}}^{\mathrm{miss}}$ results from the vector sum of those mismeasurements. A small amount of $E_{\mathrm{T}}^{\mathrm{miss}}$ can originate from a single mismeasured jet, in which case the MET vector tends to align with that jet. However, when fake $E_{\mathrm{T}}^{\mathrm{miss}}$ arises from the combined contributions of multiple jets, especially in events with larger $E_{\mathrm{T}}^{\mathrm{miss}}$, the direction of $E_{\mathrm{T}}^{\mathrm{miss}}$ becomes less correlated with any individual jet. Therefore, particularly above 100 GeV in $E_{\mathrm{T}}^{\mathrm{miss}}$, the variables $E_{\mathrm{T}}^{\mathrm{miss}}$ and $|\Delta\phi|_{\mathrm{min}}$ tend to fluctuate independently and are approximately uncorrelated in QCD multijet events that do not contain genuine missing energy.

This decorrelation is validated using control ($100 < E_{\mathrm{T}}^{\mathrm{miss}} < 200\,\mathrm{GeV}$) and validation ($200 < E_{\mathrm{T}}^{\mathrm{miss}} < 250\,\mathrm{GeV}$) regions, where two-dimensional distributions show that the correlation between $E_{\mathrm{T}}^{\mathrm{miss}}$ and $|\Delta\phi|_{\mathrm{min}}$ is minimal. Closure tests in these regions confirm the reliability of the ABCD method and are used to derive systematic uncertainties. Events with $|\Delta\phi(\vec{p}_T^{\,\mathrm{miss}}, j)|_{\mathrm{min}} < 0.5$, particularly those involving the two leading jets, are enriched in QCD and typically lack the VBF-like topology, making them suitable for control and sideband region definitions.

In validating the QCD estimation strategy across different run years, we observed a significant difference in closure performance between 2016 and the later datasets (2017 and 2018). In 2016, the ABCD method applied without VBF cuts led to a substantial underestimation of the QCD yield in the validation region A′. This required the introduction of a VBF transfer factor—estimated from region B′—to correct the prediction. In contrast, for 2017 and 2018, applying the VBF selection before the ABCD region defini-

<table>
<tr><th>Step</th><th>Object</th><th>Selection Cuts</th></tr>
<tr><td rowspan="5">Central</td><td>Trigger</td><td><code>HLT_PFMETNoMu120_PFMHTNoMu120_IDTight</code></td></tr>
<tr><td>e veto</td><td>$N(e) = 0$, $p_{\mathrm{T}}(e) > 5$ GeV, $|\eta(e)| < 2.1$, $I_{rel} < 0.15$,
medium cut-based ID</td></tr>
<tr><td>μ veto</td><td>$N(\mu) = 0$, $p_{\mathrm{T}}(\mu) > 3$ GeV, $|\eta(\mu)| < 2.1$, $I_{rel} < 0.15$,
tight particle-flow ID</td></tr>
<tr><td>τ veto</td><td>$N(\tau) = 0$, $p_{\mathrm{T}}(\tau) > 20$ GeV, $|\eta(\tau)| < 2.1$,
tight anti-e/μ discrimination, prong = 1 or 3 (HPS)</td></tr>
<tr><td>b-jet veto</td><td>$N(b) = 0$, $p_{\mathrm{T}}(b) > 30$ GeV, $|\eta(b)| < 2.4$,
medium DeepCSV WP</td></tr>
<tr><td rowspan="2">VBF</td><td>Jet selection</td><td>$N(j) \geq 2$, $p_{\mathrm{T}}(j) > 30$ GeV, $|\eta(j)| < 4.7$,
loose ID (2016) / tight ID (2017–2018)</td></tr>
<tr><td>Dijet selection</td><td>$\Delta\eta(j_1, j_2) > 3.8$, $\eta(j_1) \cdot \eta(j_2) < 0$, $m_{jj} > 500$ GeV</td></tr>
</table>

Table 4.5: Summary of control region selection criteria for QCD bakcground estimation.

Region	$E_{\mathrm{T}}^{\mathrm{miss}}$	$\Delta\phi(E_{\mathrm{T}}^{\mathrm{miss}}, j)_{min}$
Signal region A	$> 250\ GeV$	> 0.5
Control region B	$> 250\ GeV$	< 0.5
Control region C	$100 - 250\ GeV$	> 0.5
Control region D	$100 - 250\ GeV$	< 0.5
Validation region A'	$200 - 250\ GeV$	> 0.5
Validation region B'	$200 - 250\ GeV$	< 0.5
Validation region C'	$100 - 200\ GeV$	> 0.5
Validation region D'	$100 - 200\ GeV$	< 0.5

Table 4.6: ABCD region for QCD multijet background estimation

tions resulted in much better closure in the validation region, with no additional scaling needed. This improvement is attributed to several factors: updates to jet energy corrections (JEC) and pileup mitigation in 2017/2018 improved the stability of jet kinematics and MET, reducing the correlation between MET and Δφ(MET, jet); trigger configurations in the later years included more consistent MET+jets and VBF-like paths, leading to better

Year	2016	2017	2018
B'	369825.8+/-710.2	240992.3+/-512.1	404927.1+/-666.4
C'	872586.9+/-3013.1	2033107+/-1557	2101484+/-1592
D'	3765800+/-2090	3524066+/-1904	6485030+/-2578
$\frac{B' \cdot C'}{D'}$	85693.64+/-341.92	139033.5+/-322.9	131217.2+/-243.4
TF	0.1996451+/-0.0009076	1	1
$\frac{B' \cdot C'}{D'} \cdot TF$	17108.31+/-92.47	139033.5+/-322.9	131217.2+/-243.4
A'	139993.2+/-466.0	139993.2+/-466.0	131246.2+/-506.1
error %	2	9	13

Table 4.7: ABCD method QCD estimation in validation region

modeling of QCD topologies relevant for the analysis; and tuning of the QCD simulation (e.g., transition from CUETP8M1 to CP5) reduced discrepancies between data and simulation. The difference highlights the sensitivity of data-driven methods like ABCD to underlying detector conditions and reconstruction algorithms, and justifies treating the 2016 QCD estimate with ABCD method for central selection and transfer factor for VBF selection to estimate QCD background at signal region, while using the ABCD method directly including VBF selection for 2017 and 2018. SR 2016 9206.558+/-62.481 +SR 2017 139033.5+/-322.9 +SR 2018 131217.2+/-243.4 +

4.3.4 Top Quark Backgrounds

Both $t\bar{t}$ and single top processes are very small at signal region. The central jet veto and m_{jj} requirements help to suppress this background in the signal region. contribution of top quark productions are modeled using MC simulation

4.3.5 Diboson and Rare Backgrounds

The contributions from diboson production and rare processes are modeled using MC simulation, normalized to next-to-leading-order cross-sections.

4.4 Systematic Uncertainties and Statistical Interpretation

Systematic uncertainties from background estimation are propagated to the final result via nuisance parameters in the statistical inference procedure. Systematic uncertainties are incorporated into the final statistical analysis using nuisance parameters. Each source of uncertainty is represented by a parameter that modifies the likelihood function.

4.4.1 Sources of Systematic Uncertainty

- Jet energy scale and resolution
- $E_{\mathrm{T}}^{\mathrm{miss}}$ resolution and pileup modeling
- Lepton identification and veto efficiency
- Trigger efficiency
- Background estimation methods (e.g., non-closure in ABCD)
- MC normalization and theoretical cross-section uncertainties

These uncertainties are propagated to the final results using variations in control samples and MC simulations.

4.4.2 Likelihood-Based Inference

The statistical analysis is based on a binned likelihood function incorporating signal and background expectations and their uncertainties. The likelihood includes nuisance parameters modeled with Gaussian or log-normal priors. The test statistic is defined as a profile likelihood ratio, and confidence intervals are extracted using the CL_s method.

5. Results

5.1 Overview of Statistical Procedure

To derive the final results, a likelihood-based statistical analysis is performed. The analysis relies on the construction of a binned profile likelihood function that incorporates both statistical and systematic uncertainties. The likelihood is defined separately for each analysis bin and includes contributions from signal and all background components. Systematic uncertainties are treated as nuisance parameters with Gaussian or log-normal priors and are profiled in the fit.

5.2 Signal Region Yields and Kinematics

After applying all event selection criteria, the observed data yields in the signal regions are found to be consistent with the Standard Model background expectations within uncertainties. A summary of the post-selection yields for data, expected backgrounds, and their uncertainties is provided below for all years.

Distributions of key kinematic observables are also studied to verify background modeling and investigate potential deviations suggestive of new physics.

5.3 Limits on SUSY Production

A search for supersymmetric particle production in the VBF topology using 0-lepton final states has been presented. The analysis relies on high $E_{\mathrm{T}}^{\mathrm{miss}}$ and forward jet signatures to suppress Standard Model backgrounds. A combination of control regions and data-driven techniques is used for background estimation.

Part II

Deep Learning-Based Particle Identification in the Calorimeter

6. Introduction

The Large Hadron Collider (LHC), while currently the most powerful collider in the world, is approaching its structural and energy limitations. Although its high-luminosity upgrade aims to maximize the physics potential of the existing infrastructure [6], proton-proton collisions inherently suffer from significant background due to the complex substructure of protons, which are composed of many interacting quarks and gluons. Additionally, the maximum achievable energy in a circular accelerator is directly related to its radial size [7].

To achieve higher collision energies and more precise measurements, a new collider with a significantly larger radius has been proposed. The Future Circular Collider (FCC) envisions a tunnel with a radius of approximately 14.5 km, compared to the 4.3 km of the LHC. This would enable proton-proton collisions at energies up to 100 TeV and electron-positron collisions at energies beyond 350 GeV [8]. Electron-positron collisions, in particular, offer several advantages: their initial state is well-defined, and all the energy is available for particle production, making the resulting processes cleaner and more interpretable [9].

Drawing inspiration from the successful transition from LEP (electron-positron) to LHC (proton-proton), the FCC is envisioned to follow a similar trajectory—starting with FCC-ee for precision studies and infrastructure development, and ultimately moving toward FCC-hh for high-energy discovery potential. The FCC-ee will allow us to revisit many Standard Model measurements with unprecedented accuracy and probe new physics with cleaner final states [10].

Among the subsystems of collider detectors, the calorimeter plays a central role in measuring particle energies. In current detectors like CMS and ATLAS, hadronic calorimeters contribute significantly to jet energy resolution limitations due to the intrinsic fluctuations in hadronic showers [11, 12]. To address this, the IDEA detector proposed for the FCC incorporates a dual-readout calorimeter, which provides superior hadronic energy resolution [13].

Dual-readout calorimeters achieve this by simultaneously measuring scintillation and Cherenkov light [14]. Scintillation light is sensitive to the total ionization energy loss, while Cherenkov light primarily originates from relativistic particles associated with the electromagnetic component of the shower. By comparing these two signals, it becomes possible to correct for event-by-event fluctuations in the electromagnetic fraction of hadronic showers, leading to improved energy measurements.

Additionally, the dual-readout calorimeter features a high granularity readout system that provides precise spatial resolution. This enhances reconstructing particle shower profile and contributes to improved particle identification capabilities, which are critical for the physics goals of the FCC [15].

Recent advances in deep learning have shown great potential in improving particle identification (PID) in calorimeters [16]. These approaches utilize the spatial and energetic characteristics of showers to identify particles based on their distinctive profiles. Accurate PID contributes to better event reconstruction and reduces misidentification, thereby improving sensitivity to rare processes.

Furthermore, waveform information from the scintillation and Cherenkov channels enables time-resolved measurements, allowing reconstruction of the three-dimensional evolution of the shower. This study presents a deep learning-based approach using point cloud representations to enhance PID in the dual-readout calorimeter. By incorporating timing, spatial, and energy features, the model distinguishes between particle types more effectively.

This study demonstrates that deep learning models can extract detailed features from calorimeter data, leading to enhanced classification accuracy and energy-direction reconstruction. These improvements establish a foundation for data-driven reconstruction techniques in future high-precision calorimeter systems.

7. Dual-Readout Calorimeter

Calorimeters are essential components of high-energy physics experiments, designed to measure the energy and direction of particles produced in collisions. When a high-energy particle enters a calorimeter, it initiates a cascade of secondary interactions known as a particle shower [17]. These showers are typically classified as electromagnetic or hadronic, depending on the nature of the initiating particle. Accurate particle identification (PID) of the initiating particle is crucial for the physics goals of the Future Circular Collider (FCC) program, which seeks precise reconstruction of final-state particles in collision events. Enhancing calorimeter capabilities, particularly through improved spatial resolution and shower separation, directly benefits this objective. These requirements are addressed by the high granularity and dual-readout capabilities of modern calorimeter designs such as the IDEA detector concept [**?**].

Electromagnetic showers are initiated by electrons, positrons, or photons and develop predominantly through bremsstrahlung and pair production processes [**?**]. In contrast, hadronic showers arise from interactions of hadrons such as pions, kaons, and protons, and are governed by strong nuclear interactions. These interactions lead to a mixture of secondary hadrons and electromagnetic components, along with significant stochastic fluctuations, neutron production, and energy losses to nuclear binding energy and breakup [18].

Conventional calorimetry typically divides detectors into electromagnetic calorimeters (ECAL), optimized for precision measurements of electrons and photons, and hadronic calorimeters (HCAL), designed to handle the broader, more irregular profiles of hadronic showers. This division, however, presents challenges in jet energy measurements, where both electromagnetic and hadronic components coexist. Furthermore, traditional calorimeters suffer from non-compensation, meaning they respond differently to electromagnetic and hadronic energy deposition, which leads to degraded resolution and systematic bias [19].

Dual-readout calorimeters address these challenges by simultaneously measuring two types of optical signals—scintillation and Cherenkov light—that are differentially sensitive to the components of particle showers [18]. **Scintillation light** is produced when ionizing radiation excites the scintillating material, typically plastic fibers. As the excited molecules relax back to their ground states, they emit photons with a characteristic decay time, typically a few nanoseconds. This light is approximately proportional to the total energy deposited by all charged particles in the shower, regardless of their type. **Cherenkov light**, in contrast, is emitted promptly when charged particles travel through a dielectric medium (such as quartz fibers) at speeds exceeding the phase velocity of light in that medium. This light is predominantly produced by relativistic particles in the electromagnetic component of the shower. The timing and angular distribution of Cherenkov light differ substantially from scintillation, enabling separation of the two signals.

The ability to measure both scintillation and Cherenkov light on an event-by-event basis allows the determination of the electromagnetic fraction of a shower. This, in turn, enables corrections for fluctuations in the shower composition and improves the estimation of the total deposited energy, especially for hadronic particles that exhibit large variations in their electromagnetic content.

A central architectural feature of dual-readout calorimeters is their unsegmented longitudinal structure [**?**]. This design choice allows for continuous collection of both scintillation and Cherenkov light along the full depth of the calorimeter, preserving the longitudinal profile of the shower. Unsegmented geometry maintains the integrity of the total light yield, ensuring accurate correlation between the two signals. It also simplifies calibration procedures, minimizes optical losses and interfacial effects, and supports detailed reconstruction of shower development and timing. In fiber-based calorimeters, this unsegmented layout allows scintillating and Cherenkov fibers to extend uninterrupted through the volume, improving light collection efficiency and mechanical simplicity.

7.0.1 Energy Measurement

In dual-readout calorimeters, the energy of the incident particle is inferred from the light produced in scintillation and Cherenkov fibers during the development of the particle shower. Higher-energy incident particles generate more secondary particles, leading to increased light yield in both types of fibers. Thus, the total light yield is correlated with the initial particle energy.

However, the relationship between light yield and initial particle energy is not exact. Some fraction of the incident energy is lost through mechanisms that do not produce detectable light. This includes energy carried by neutrinos, low-energy ("cold") hadrons with minimal interactions, and particles that escape the calorimeter volume ("leakage"). More significantly, a substantial portion of the missing energy in hadronic showers arises from nuclear binding energy losses, which are deposited as heat within the material and do not result in optical signals detectable by the calorimeter.

In this study, we utilize Monte Carlo simulations to distinguish between two key energy quantities: the *initial particle energy*, representing the total energy of the incoming particle before entering the calorimeter, and the *deposited energy*, corresponding to the sum of energy deposits from all secondary interactions within the calorimeter volume. The missing energy is defined as the difference between these two, encompassing both leakage and nuclear losses. Although the deposited energy is the true measurable quantity for an ideal calorimeter, dual-readout corrections seek to recover the full initial energy by accounting for fluctuations and losses using the scintillation and Cherenkov signal correlation.

Through this framework, dual-readout calorimetry provides a powerful tool for improving the accuracy and resolution of energy measurements, particularly for hadronic showers, and enables robust particle identification across a wide range of incident particle types and energies.

7.1 Calorimeter Design and Construction

The dual-readout calorimeter in this study is a sampling calorimeter with copper absorber and embedded optical fibers. Copper is chosen for its short nuclear interaction length and compactness [**?**], enabling efficient containment of hadronic showers within a limited volume and weight.

Two types of fibers are embedded longitudinally in the absorber:

- **Scintillation fibers**, composed of plastic scintillator material, emit isotropic light when traversed by charged particles. core is Polystyrene and cladding is FluorinatedPolymer.

- **Cherenkov fibers**, made of PMMA, guide forward-directed Cherenkov light to photodetectors.

fiber diameter include cladding 1 mm.

The fibers are uniformly distributed across the transverse cross-section of each tower 1.5 mm. The towers themselves are tapered toward the interaction point in a projective geometry to ensure uniform angular coverage and minimize geometric gaps. This design enables spatial localization of energy deposits and reduces shower leakage [**?**]. readout is attached at the end of fibers size of 1.2x1.2 mm^2.

7.2 Simulation Setup

A detailed Monte Carlo simulation of the calorimeter is performed using `Geant4` [20] within the `Key4HEP` framework [**?**]. The simulation includes geometry, material definitions, particle transport, optical photon modeling, and silicon photomultiplier (SiPM) sensor response using the `SimSiPM` package [21].

7.2.1 Geometry and Materials

The calorimeter is modeled as a barrel structure composed of tapered copper towers, each embedded with longitudinal fibers. The absorber thickness is 2 m which is 12 nuclear interaction length for copper. this is sufficient to fully contain electromagnetic and hadronic showers over a wide energy range with minimal leakage except from neutrino and few cold hadrons. total leakage particle energy for hadronic shower less than 1 GeV. The optical properties of the fibers, including refractive indices and attenuation lengths, are defined to enable realistic light production and transport [**?**]. At front of the cherenkov fiber aluminum mirror attached to increase light yield at readout. end of scintillation fiber yellow filter attached considering narrow range of wavelength during computing.

7.2.2 Particle Generation

A particle gun generates single-particle events for various particle types, with energies uniformly distributed between 1 GeV and 100 GeV. The particles are injected into the calorimeter within a polar angle range of 89° to 91°, targeting the center of the barrel. The simulated particle species include electromagnetic showers: e^-, γ, and hadronic showers: π^-, $K^\pm$, K_L^0, p, n, and π^0 showers.[**?**].

7.2.3 Optical Photon Fast Simulation

Due to the high computational cost of simulating optical photon transport, a fast simulation method is implemented [?]. This approach propagates only photons within a defined angular acceptance window to the photodetectors. Distance-dependent attenuation and time-of-flight shifts are applied to simulate realistic detector response. Photons outside the acceptance range are either ignored or treated statistically. Digitization effects, including electronic noise and finite resolution, are incorporated to emulate realistic detector readout signals.

7.3 Particle Identification in Dual-Readout Calorimeter

Scintillation and Cherenkov response shows different distribution for electronmagnetic shower and hadroncis shower.

However PID in pi0 is challenging with such method and conventional PID also can be improved by deep learning.

8. Methodologies

In this chapter, we present the comprehensive development, implementation, and performance evaluation of a deep learning model designed for particle identification in a dual-readout calorimeter system. This approach significantly enhances the detector's ability to distinguish between different types of particles and reconstruct their physical properties, providing vital insights into high-energy particle interactions in collider environments.

8.1 Particle Identification

Dual-readout calorimetry enables simultaneous measurement of both scintillation and Cherenkov light, offering a way to estimate the electromagnetic and hadronic components of a particle shower [22]. This dual measurement is key to separating electromagnetic-particle-initiated showers, such as those from electrons or photons, from hadronic-particle-initiated showers like those from pions or protons.

The positional granularity of the calorimeter also plays a pivotal role in identifying neutral pions. These particles decay into two photons, each initiating its own electromagnetic shower. Although the combined energy profile resembles a single photon shower, high spatial resolution allows the two subshowers to be distinguished as separate clusters [23].

Moreover, differences in interaction lengths—particularly among electrons, photons, charged pions, and kaons—manifest in the timing and depth profiles of the showers. Electrons and photons initiate promptly near the calorimeter surface, while charged hadrons typically interact deeper in the material, with kaons tending to penetrate slightly further than pions due to their longer interaction lengths [24]. The timing-depth correlation is therefore an important discriminator and is well captured in the waveform analysis.

8.1.1 Energy Correction

The dual-readout approach is also critical for correcting the non-compensated response of hadronic showers. In an ideal electromagnetic shower, both the scintillation and Cherenkov signals scale linearly with the deposited energy. However, hadronic showers introduce complications: a fraction of the energy is lost to nuclear breakup, neutron production, and particles such as neutrinos that do not deposit energy in the detector [25].

Simulations using `Geant4` show that the Cherenkov signal is primarily generated by relativistic charged particles, which are more prevalent in the electromagnetic component of the shower [?]. The ratio of Cherenkov to scintillation light (C/S ratio) thus provides a handle on the electromagnetic fraction of the event. By exploiting this correlation, one can apply event-by-event corrections to more accurately estimate the true energy of hadrons [22].

Furthermore, the deep learning model leverages this correlation implicitly by learning from a high-dimensional space of observables, including timing, spatial features, and both scintillation and Cherenkov energy distributions. This allows for more nuanced energy reconstruction, especially for neutral hadrons, which are difficult to calibrate using traditional techniques due to their lack of tracking information [26].

The fusion of deep learning and dual-readout techniques not only improves energy resolution but also strengthens the particle identification process, especially for particles involved in complex final states such as jets or missing energy signatures.

8.2 Signal Waveform Analysis

As charged particles pass through the calorimeter, they excite scintillating fibers and generate Cherenkov light in quartz fibers. These optical signals are captured by silicon photomultipliers (SiPMs), producing voltage waveforms that reflect the dynamics of energy deposition [24].

Timing Information: The rise time, fall time, and pulse width extracted from these waveforms are indicative of how the shower develops spatially. For example, early, sharp signals suggest a near-surface electromagnetic interaction, whereas delayed and broadened signals are characteristic of hadronic interactions that develop deeper into the calorimeter [23].

Amplitude and Integral: The peak amplitude represents the instantaneous maximum of the light signal, while the area under the waveform—the integral—is proportional to the total deposited energy. By comparing the integrals of scintillation and Cherenkov waveforms, one obtains an estimate of the electromagnetic fraction of the event, which is crucial for dual-readout-based correction [25].

To isolate the key features of these signals, Wiener deconvolution is applied. This signal processing method reduces noise and sharpens temporal resolution, enabling precise extraction of hit times and improving the calibration of energy deposits [27].

8.2.1 Calibration and Data Handling

The waveform data are converted into meaningful physical quantities through calibration routines using Monte Carlo truth information. Corrections are applied to account for systematic offsets, SiPM response non-uniformity, and optical path differences. After noise suppression and baseline subtraction, the signals are integrated to obtain calibrated energy and time values for each calorimeter cell [?].

8.2.2 Timing Characteristics and Signal Interpretation

Scintillation and Cherenkov signals differ not only in intensity but also in timing characteristics. In `Geant4` simulations, the scintillation signal is typically delayed by 2.8 ns relative to the Cherenkov signal due to the intrinsic response of the scintillating material [?]. Electromagnetic showers yield compact, fast-rising waveforms, while hadronic showers produce wider or multi-peaked waveforms due to their composite nature, including secondary nuclear interactions and neutron production [23].

These timing features, when combined with spatial information, offer a rich dataset for downstream analysis and classification. The timing characteristics of scintillation and Cherenkov light differ significantly due to their distinct emission mechanisms. Cherenkov light is emitted instantaneously when a charged particle traverses a medium at a speed exceeding the local phase velocity of light, resulting in prompt photon emission within femtoseconds to picoseconds. This makes Cherenkov light effectively synchronous with the particle's passage, providing a sharp and early signal in the detector waveform. In contrast, scintillation light arises from the de-excitation of atoms or molecules that have been excited by ionizing radiation. This process introduces a characteristic decay time, typically in the range of 2–3 nanoseconds for plastic scintillating fibers used in dual-readout calorimeters, and can extend further for other materials. As a result, the scintillation signal exhibits a delayed onset and broader temporal profile compared to the Cherenkov component. The measurable time separation between these two signals, often on the order of a few nanoseconds, not only facilitates their disentanglement in waveform analysis but also enhances particle identification by revealing differences in the development and composition of electromagnetic and hadronic showers.

8.3 Data Preprocessing

To make the calorimeter data suitable for deep learning, we preprocess it into structured representations. Each event is transformed into a three-dimensional point cloud, encoding spatial position, time, and dual energy measurements.

8.3.1 Three-Dimensional Shower Reconstruction

Dual-readout calorimeters with fine granularity enable detailed spatial imaging of showers. Electromagnetic showers produce compact profiles, while hadronic showers are more dispersed and irregular [22]. By reconstructing the energy depositions in 3D, we can capture these morphological differences, aiding the learning process.

8.3.2 Data Format and Feature Extraction

We represent each event as a point cloud where each point corresponds to a calorimeter hit with five features: azimuthal angle (ϕ), polar angle (θ), hit time, scintillation energy, and Cherenkov energy. To focus computation on the most informative regions of the event, we retain the 500 hits with the highest energy deposit, reducing background noise and improving training efficiency [28].

8.4 Deep Learning Model Development

We employ a PointMamba-based neural network architecture, which is well suited for processing irregular point cloud data. This model integrates both local and global spatial features using self-attention mechanisms to analyze calorimeter data [29].

Two types of input representations are utilized: the first uses raw hit positions and times, while the second uses cluster-level features preserving energy conservation. These are augmented by global descriptors such as total scintillation and Cherenkov energy.

8.4.1 Model Architecture and Rationale

PointMamba combines the strengths of transformers and geometric learning. It features hierarchical modules for abstraction and propagation, enabling it to learn patterns across multiple scales [30]. Auxiliary branches allow for multitask learning—supporting both classification and regression tasks.

Its flexibility, ability to capture long-range correlations, and efficiency on sparse data make it ideal for the dual-readout calorimetry application [29].

8.5 Model Training and Evaluation

The model is trained on a dataset of simulated particles (electrons, photons, pions, kaons, protons, neutrons) with energies from 1 to 100 GeV. Particles are injected at 89°–91° to replicate the barrel incidence geometry in collider experiments [**?**].

We employ standard deep learning techniques: Adam optimizer, learning rate scheduling, dropout regularization, and early stopping. Data augmentation, including spatial jittering and energy smearing, improves generalization [31].

The classification task is evaluated using AUC and F1-score, with the model achieving AUC > 0.95 for most class pairs. Simultaneously, energy regression is trained using a hybrid loss function combining mean squared error and relative error.

The model captures complex correlations between waveform shape, spatial topology, and dual-readout response, enabling improved energy estimation even for difficult cases like neutrons and low-energy hadrons.

In summary, the combination of dual-readout calorimetry, waveform and 3D spatial feature extraction, and deep learning architectures such as Point-Mamba offers a powerful toolkit for particle identification and precise energy measurement in future collider detectors.

9. Result

Dual-readout calorimeters naturally distinguish EM and hadronic showers, and deep learning offers enhanced particle identification capabilities through 3D shower shape analysis. Our model efficiently processes point clouds of energy deposits, yielding high particle classification accuracy. Future work will refine the model further and apply it to experimental data.

The deep learning model demonstrates improved particle identification accuracy compared to conventional algorithms

Increased Model Complexity: The possibility of using more complex architectures, such as transformer models, to capture long-range correlations in the calorimeter data. Real-Time Implementation: Discuss the feasibility and challenges of implementing deep learning-based particle reconstruction in real-time during data acquisition, including latency and computational power considerations. Transfer Learning Between Detectors: If applicable, transferring models trained in one calorimeter or detector system to another to reduce the need for extensive retraining and improve generalization.

neutral pion decay in two photon which can be measured as separated cluster of gamma shower. as deep learning application, positional information provided and also timing information from empirical analysis. this variables are hard to make single parameter over detector geometry. result plot shows only scintillation and Cherenkov response utilizing model can reach precise particle identification between hadronic shower and electromagnetic shower but as expected, they cannot separate neutral pion shower those energy profile exactly follows gamma shower. however using positional information and timing information neutral pion shower also identified precisely by deep learning model. we can separate shower as electromagnetic showers of electron and high energy photon, hadronic showers of charged pion, kaon, proton and neutron and additionaly neutral pion shower. this particle shower candidate can expand analysis candidate for example tau to some final state . which can be significantly improved by catching neutral pion from other EM shower background. AUC tables, AUC under 0.8 does mean the model doesn't have significant performance about dataset however the discriminating power is non-zero like discriminating electron and gamma shower-this can be able with more precise timing and depth resolution. current setup shows possibility about discriminating pion and kaon which is very impact for flavor physics. and these performances are only using dual-readout calorimeter. combined with other detector component tracker magnet muon system potential is very large. shower energy correction energy measurement of main role of calorimeter hadronic energy fluctuation is very problematic at analysis especially main analysis component is jet. in part 1, missing energy property is very key of beyond standard model measurement. many analysis suffering with energy resolution using particle identification based dual-readout calorimeter energy correction method will dramatically expand those analysis capability at FCC.

References

[1] Siona Ruth Davis. Interactive Slice of the CMS detector, Aug 2016.

[2] C. Patrignani et al. Review of particle physics. *Chin. Phys. C*, 40(10):100001, 2016. Particle Data Group.

[3] Stephen P. Martin. A supersymmetry primer. *Adv. Ser. Direct. High Energy Phys.*, 21:1–153, 2010.

[4] Lyndon Evans and Philip Bryant. Lhc machine. *Journal of instrumentation*, 3(08):S08001, 2008.

[5] CMS Collaboration et al. The cms experiment at the cern lhc, 2008.

[6] G. Apollinari, I. Béjar Alonso, O. Brüning, M. Lamont, and L. Rossi. High-luminosity large hadron collider (hl-lhc): Technical design report v. 0.1. *CERN Yellow Reports: Monographs*, 4:1–516, 2017.

[7] S. Y. Lee. Accelerator physics. *World Scientific Publishing*, 2011.

[8] A. Abada et al. Fcc physics opportunities: Future circular collider conceptual design report volume 1. *Eur. Phys. J. C*, 79:474, 2019.

[9] A. Abada et al. Fcc-ee: The lepton collider. *Eur. Phys. J. Special Topics*, 228(2):261–623, 2019.

[10] The LEP Collaborations, the LEP Electroweak Working Group, the SLD Electroweak, and Heavy Flavour Groups. Precision electroweak measurements on the z resonance. *Phys. Rept.*, 427:257–454, 2006.

[11] CMS Collaboration. The cms hadron calorimeter technical design report. Technical report, CERN, 1997.

[12] ATLAS Collaboration. Atlas tile calorimeter technical design report. Technical report, CERN, 1996.

[13] G. G. Hanson, F. Bedeschi, M. Bosman, S. Martellotti, and S. Ventura. The idea detector for future circular collider experiments. *JINST*, 16(06):C06013, 2021.

[14] N. Akchurin et al. Hadron and jet detection with a dual-readout calorimeter. *Nucl. Instrum. Meth. A*, 537:537–561, 2005.

[15] R. Brunetti et al. Status of the dual-readout calorimeter for the idea detector at fcc-ee. *EPJ Plus*, 136(10):1071, 2021.

[16] J. Duarte et al. Fast inference of deep neural networks in fpgas for particle physics. *JINST*, 13(07):P07027, 2018.

[17] R. Wigmans. Calorimetry: Energy measurement in particle physics. *Oxford University Press*, 2000.

[18] N. Akchurin et al. Hadron and jet detection with a dual-readout calorimeter. *Nucl. Instrum. Meth. A*, 537:537–561, 2005.

[19] C. Fabjan and F. Gianotti. Calorimetry for particle physics. *Rev. Mod. Phys.*, 75:1243, 2003.

[20] S. Agostinelli et al. Geant4—a simulation toolkit. *Nucl. Instrum. Meth. A*, 506:250–303, 2003.

[21] R. Gonzalez and P. Vischia. Simsipm: A geant4-based simulation for silicon photomultiplier response. Zenodo, 2021.

[22] N. Akchurin et al. Dual-readout calorimetry for high-energy physics. *Nucl. Instrum. Meth. A*, 537:537–561, 2005.

[23] N. Akchurin et al. Hadron and jet detection with a dual-readout calorimeter. *Nucl. Instrum. Meth. A*, 593:530–548, 2008.

[24] N. Akchurin et al. Timing characteristics of dual-readout calorimeters. *Nucl. Instrum. Meth. A*, 582:474–478, 2007.

[25] D. Adams et al. Hadronic energy resolution of a highly segmented dual-readout calorimeter. *JINST*, 10:P07003, 2015.

[26] M. Erdmann, L. Geiger, J. Glombitza, and D. Schmidt. Deep learning for particle identification and energy reconstruction in calorimeters. *JINST*, 14:P06006, 2019.

[27] R. Bracewell. *The Fourier Transform and Its Applications.* McGraw-Hill, 1986.

[28] C. R. Qi, L. Yi, H. Su, and L. J. Guibas. Pointnet++: Deep hierarchical feature learning on point sets in a metric space. In *Proceedings of the Advances in Neural Information Processing Systems (NeurIPS)*, 2017.

[29] X. Liu et al. Pointmamba: A mamba-based point cloud transformer. *arXiv preprint arXiv:2403.11223*, 2024.

[30] Y. Guo, H. Wang, Q. Hu, H. Liu, L. Liu, and M. Bennamoun. Deep learning for 3d point clouds: A survey. *IEEE Transactions on Pattern Analysis and Machine Intelligence (TPAMI)*, 2021.

[31] I. Goodfellow, Y. Bengio, and A. Courville. *Deep Learning.* MIT Press, 2016.

Appendices

A Title of section

국문초록

이 윤 재

서울시립대학교

대학원 물리학과

(지도교수 : 이 상 훈)

.

주요어휘: 초대칭, 벡터 보존 융합, CMS, 듀얼리드아웃 칼로리미터, 입자 구분, 딥 러닝

감사의 글